Disorder characterization of porous media and its effect on fluid displacement

Zhongzheng Wang,[1,2] Kapil Chauhan,[1] Jean-Michel Pereira,[2] and Yixiang Gan[1,*]
[1]*School of Civil Engineering, The University of Sydney, NSW 2006, Australia*
[2]*Laboratoire Navier, UMR 8205, Ecole des Ponts ParisTech, IFSTTAR, CNRS, UPE, France*

(Received 19 December 2018; published 29 March 2019)

We investigate the effects of topological disorder and wettability on fluid displacement in porous media. A modified disorder index I_v is proposed to characterize the disorder of porous media. By changing I_v, different displacement patterns (stable displacement and fingering) under the same flow condition and fluid property are obtained. We analytically demonstrate how increase in disorder promotes fingering due to uneven distribution of local capillary pressure. It is shown that the displacement efficiency for different wettability conditions and disorder well correlates with the distribution of local capillary pressure. A power-law relation between fluid-fluid interfacial length and saturation of invading fluid is proposed by taking geometry into account, where the parameters in power-law relation can be predicted by the capillary index, I_c, unifying the effects of topological disorder and wettability.

DOI: 10.1103/PhysRevFluids.4.034305

I. INTRODUCTION

Displacement of multiphase fluids in porous media is involved in many industrial and natural processes, such as injection of CO_2 into geological formations [1,2], enhanced oil recovery [3,4], remediation of contamination in aquifer systems [5], and water infiltration into soil [6]. Studies have been conducted with a focus on impacts of flow conditions and fluid properties on displacement of multiphase flows [7,8], and effects of gravity [9] and wettability [10–12], while less attention has been paid on correlating the pore-scale disorder of porous media with the fluid displacement.

The displacement patterns, including capillary fingering (CF), viscous fingering (VF), and stable displacement (SD), are primarily controlled by capillary number, Ca, and viscosity ratio, M, between the defending and invading fluids [13–18]. When the invading fluid is more viscous than the defending fluid, i.e., $M < 1$, the displacement patterns tend to shift from SD to CF with the decrease of Ca, indicating the dominance of the interfacial tension. While in the case of $M > 1$, increase of Ca modifies the flow toward VF. At the same time, wettability is also proven to play an important role: Increasing contact angle of invading fluid results in more efficient displacement at all Ca [19–21], but when the contact angle exceeds a critical value, the trend is reversed due to *corner flow* [12].

Another important factor that influences fluids displacement is disorder of the porous media. For flows dominated by capillary effects (low Ca), increase in disorder promotes fingering, leading to a transition from SD to CF [10,22]. While for large Ca with $M > 1$, high disorder modifies the viscous fingerings to become more chaotic instead of having ordered patterns in regular media [13]. When both capillary and viscous effects are important, Holtzman [23] found that increase in disorder leads to higher interfacial area and lower displacement efficiency due to trapping. Holtzman [23] also offer

*yixiaing.gan@sydney.edu.au

subtle observations on effects of disorder by considering both capillary and viscous effects through scaling analysis [23]. However, many pore-scale simulation models assume quasistatic displacement [15], thus not capable of properly simulating dynamic mechanisms which are crucial even in slowly driven systems [21]. Despite a recent improvement of pore-scale simulation on ability of capturing nonlocal nature of interface dynamics [21], some processes during multiphase flow still remain un-captured such as droplet fragmentation [24]. In addition, due to the complex interplay among fluids properties, flow conditions, and topological features, the study of disorder effects on fluid displacement remain an active area of research, and attracts increased attention in the recent years with the help of development in microfluidics and advances in computational methods.

Multiphase flow in porous media has been studied both experimentally using micromodels [12,15,16,25–27] and numerically by a range of simulation methods. Pore-network (PN) models, though computationally efficient, have limited predictive capability and accuracy due to simplification of pore geometries and/or flow equations [28–30]. Statistical models including diffusion-limited aggregation (DLA), anti-DLA, and invasion percolation (IP) have been used to simulate VF, SD, and CF, respectively. However, these "specialized" models cannot capture transitions between different regimes [18,31]. Grid-based methods with interface tracking such as volume of fluid (VOF) method and level set (LS) method have been proposed to study multiphase flow in porous media [32–36]. However, they suffer from numerical instability at the interface when interfacial tension becomes dominant for microdroplets [37]. In addition, they have only been applied to simple pore geometries due to relatively high computational costs. The lattice Boltzmann method (LBM), as a mesoscale method, has been developed into a powerful tool for flow simulation in porous media [38–42]. Comparing to other numerical methods, the LBM is particularly suitable for pore-scale simulation of multiphase flows due to its ability of handling complex geometries and also being able to be massively parallelized. Therefore, it has been applied to study many problems in fluid mechanics [43–45].

In this paper, we investigate the effects of disorder and their coupling with wettability on fluid displacement in porous media. To better describe multiphase flow in porous media, a modified disorder index I_v is proposed to characterize disordered geometry by reflecting the degree of fluctuation of local porosity. Samples are generated to have distinct values of I_v for numerical simulations using lattice Boltzmann method. Through controlling the disorder of geometry, we are able to produce different displacement patterns (stable displacement and fingering) under the same capillary number and viscosity ratio, providing new insights toward the conventional displacement phase diagram which is independent on system geometry. We demonstrate how increase in disorder collaborated with interfacial phenomena promote fingering due to uneven distribution of local capillary pressure. It is shown that for different wettability conditions and disorder, the displacement efficiency well correlates with the distribution of local capillary pressure. Finally, a power-law relation between fluid-fluid interfacial length and saturation of invading fluid is constructed. The parameters in power-law relation can be predicted by the capillary index, I_c, which combines the effects of topological disorder and wettability.

II. METHOD

A. Media generation and characterization

Our geometry is a rectangular domain filled with circular obstacles to simulate the solid phase in porous media as as as shown in Fig. 1. The porosity of the medium, defined as the ratio of void area to total area in the 2D space, is controlled by varying the diameter of the obstacles. These obstacles are initially regularly placed on a triangular lattice.

To characterize the disorder of the medium, we use similar idea from Laubie *et al.* [46] but a different calculation method: Instead of using fixed square meshing in their study of mechanical behavior of solid material (originally named as I_d), a Voronoi diagram is constructed for obtaining the local porosity, then a disorder index I_v can be defined as the corrected standard deviation of local

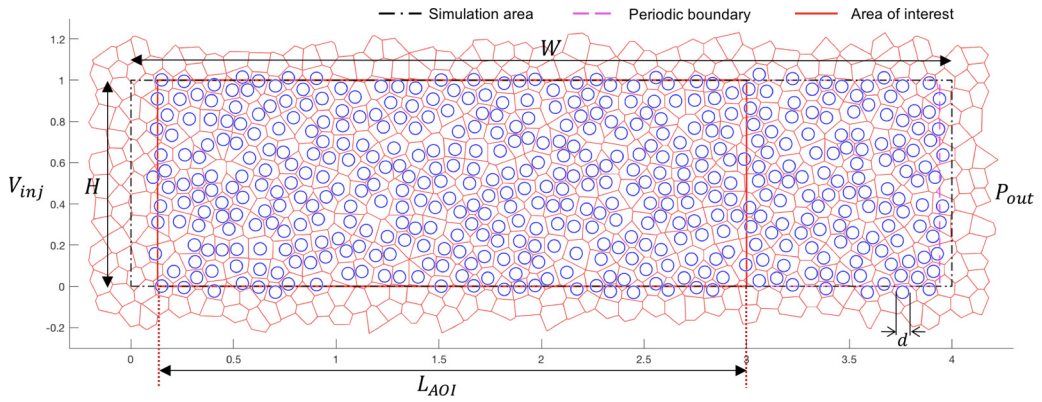

FIG. 1. Our porous medium is composed of 440 circular obstacles with diameter $d = 0.06$, which are initially regularly placed on a triangular lattice. The area enclosed by black dot-dash line is the simulated area with injection width H and longitudinal length W, while our results and analysis are based on the area of interest (L_{AOI}), which is enclosed by red solid line. Geometrical periodicity in horizontal and vertical direction is ensured inside periodic boundary (purple-dashed line). The invading fluid is injected from the left with a constant velocity V_{inj}. The pressure at the right end is set to be constant P_{out}. Periodic boundary condition is imposed at top and bottom of the simulation area.

porosity:

$$I_v = \sqrt{\frac{\sum_{n=1}^{N}(\phi_n - \bar{\phi})^2}{N-1}}, \tag{1}$$

where N is the number of obstacles in the domain, ϕ_n is the local porosity within the Voronoi cell, and $\bar{\phi}$ is the overall porosity of the medium.

Disorder is introduced by Monte Carlo iterative movement of each obstacle with an apparent diameter $D_{\mathrm{app}} = \lambda D$ with $\lambda \in [1, D_{\max}/D]$, where D is the original diameter of obstacle and $D_{\max}$ is the maximum diameter to achieve the maximum packing, e.g., ideally $\frac{\sqrt{3}\pi}{6}$ in 2D, and its value depends on the system dimension and number of obstacles. Thus, $\lambda = 1$ corresponds to a fully disordered system where no restriction is applied during perturbation except that overlap is avoided, while $\lambda = D_{\max}/D$ corresponds to a regular system where no obstacle is able to move since they are already in contact with each other according to their apparent diameter. Here, we focus on media with obstacles of same size. Periodicity is ensured in both horizontal and vertical direction for obstacle distribution and for the consequent Voronoi diagram in the periodic boundary (Fig. 1). During each time-step, perturbation is applied to each particle, after which the disorder index I_v is calculated. This process stops when I_v stabilizes around a certain value for given λ (the fluctuations in I_v are generally smaller than 5% at the end). Thus, $I_v = 0$ corresponds to a perfectly ordered system, exhibiting no variation in local porosity; whereas large values of I_v correspond to disordered systems by reflecting fluctuation of local porosity with respect to fully ordered one. We found that the disorder index I_v has a monotonic correlation with λ: as λ decreases, I_v increases and the system becomes more disordered. It is also found that the achievable maximum value of I_v is dependent on the size of system domain, total number of obstacles, and the overall porosity. With our choice of a simulation domain with a length to width ratio $W/H = 4$, and a periodic domain with $x \in [0.1299, 3.9404]$ and $y \in [0, 1]$ filled with 440 obstacles having a diameter of 0.06 (corresponding to an overall porosity of 0.6735), $I_v \in [0, 0.08]$. Using this method, five geometries with distinct disorder have been generated for simulation with $I_v = [0,\ 0.020,\ 0.036,\ 0.047,\ 0.054]$ (see Fig. 2). Generally, with increasing I_v, the medium becomes more disordered and the variations in throat sizes becomes larger.

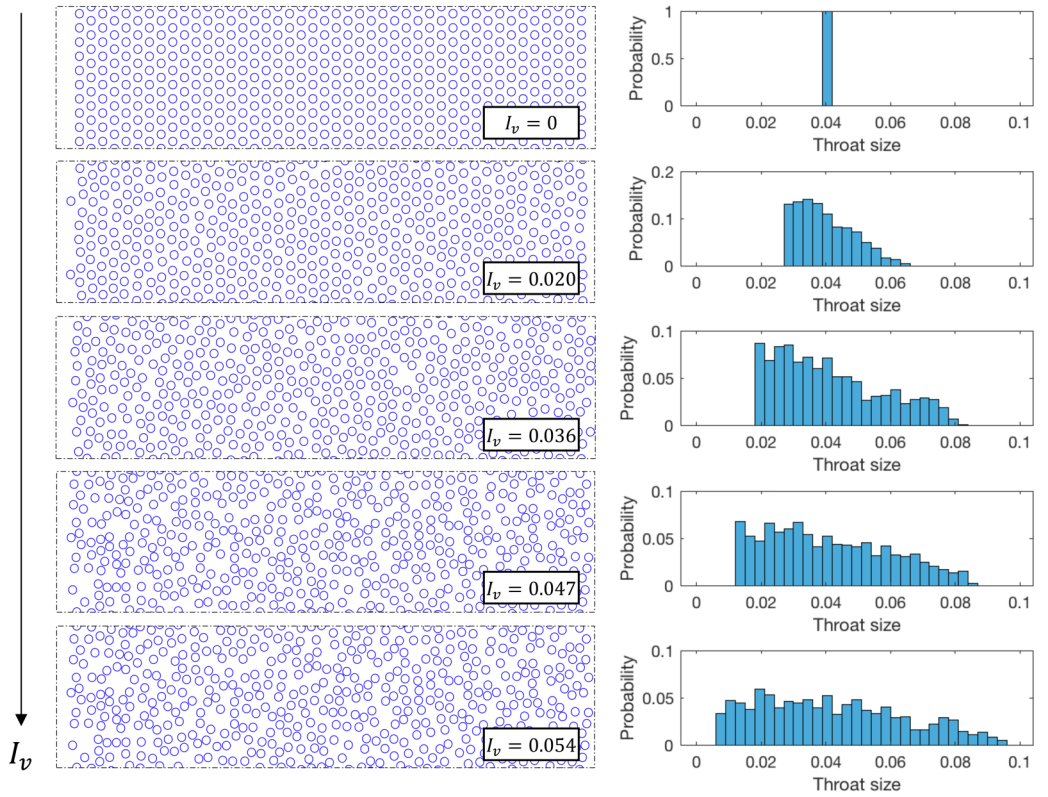

FIG. 2. Generated porous media and corresponding throat size probability distribution. From top to bottom, $I_v = 0,\ 0.020,\ 0.036,\ 0.047,\ 0.054$.

It is necessary to elaborate on reasons to introduce I_v instead of directly using λ as the disorder parameter [10,23,25,47]. First, although a monotonic relation has been observed between λ and I_v, from the definitions, λ is a parameter for generating the geometry controlling the minimum distance between obstacles, while I_v is the parameter for geometry characterization. Second, at the start of perturbation, the disorder of geometry can be quite different (usually in an increasing trend) for the same λ, until a sufficient number of iterations have passed. This is reflected by I_v having an increasing tendency followed by fluctuation around a constant value, without which it is hard to define how many iterations are "sufficient." Finally, due to the the construction of Voronoi diagram for calculating I_v, each local porosity is dependent on its proximity of adjacent obstacles. Therefore, a large I_v not only reflects the uneven spacial distribution of individual obstacles, but also implies the existence of dense clusters, which has strong influences on regional trapping as we will show in our results.

B. Simulation method

Standard lattice Boltzmann method with D2Q9 lattice is used for our 2D numerical simulations, which includes streaming and collision steps as

$$f_i(\boldsymbol{x} + \boldsymbol{c}_i \Delta t, t + \Delta t) = f_i(\boldsymbol{x}, t) + \Omega_i(\boldsymbol{x}, t), \tag{2}$$

where f_i is the density distribution function in ith direction. In this study, Bhatnagar-Gross-Krook (BGK) approach was preferred to multirelaxation time (MRT) one due to extra computational

resources and complexity required for the latter [42]. The BGK collision operator is

$$\Omega_i(\boldsymbol{x}, t) = -\frac{f_i - f_i^{\mathrm{eq}}}{\tau}\Delta t, \tag{3}$$

which relaxes the distribution function towards an equilibrium f_i^{eq} at a rate determined by the relaxation time τ. The equilibrium distribution function is given by

$$f_i^{\mathrm{eq}}(\boldsymbol{x}, t) = \omega_i \rho \left[1 + \frac{\boldsymbol{u}\cdot\boldsymbol{c_i}}{c_s^2} + \frac{(\boldsymbol{u}\cdot\boldsymbol{c_i})^2}{2c_s^4} - \frac{\boldsymbol{u}\cdot\boldsymbol{u}}{2c_s^2}\right], \tag{4}$$

where ω_i is the weight for the ith direction. We use Shan-Chen multicomponent model originally proposed by Refs. [38,39]. They introduced an interparticle force as

$$F^{\mathrm{SC}(\sigma)}(\boldsymbol{x}) = -\psi^{(\sigma)}(\boldsymbol{x}) \sum_{\bar{\sigma}\neq\sigma} G_{\bar{\sigma}\sigma} \sum_i \omega_i \psi^{(\bar{\sigma})}(\boldsymbol{x} + \boldsymbol{c_i}\Delta t)\boldsymbol{c_i}\Delta t, \tag{5}$$

where $\psi^{(\sigma)}$ is the "effective" density function for σ component, and G is a simple scalar that controls the strength of the interaction. To model immiscible fluids, the interaction strength G must be positive, simulating the repulsive force between different components. By adopting different fictitious wall densities, contact angles can be tuned [48]. Regularized boundary condition proposed by Latt and Chopard [49] is adopted to achieve second-order accuracy. For more detailed information about lattice Boltzmann method, we refer to Mohamad [50] and Kruger *et al.* [42]. We choose a mesh size of 800 × 3200 lu^2 (lu: lattice unit) for the simulation area such that at least 10 lattices are in between the smallest throat to ensure the grid is fine enough [51]. Each time after the generation of media, the minimum throat distance $r_{\min}$ is determined. To ensure minimum number of lattices $N_{\min}$ along $r_{\min}$, the number of lattices required in vertical direction for the simulation domain is calculated as $M_v = \frac{N_{\min}}{r_{\min}} \times H$, and $M_h = 4 \times M_v$ for horizontal direction, where H is the height of the simulation domain shown in Fig. 1. Note that this method assumes $r_{\min}$ and principal directions can be aligned. For example, with $N_{\min} = 10$ and $r_{\min} = 0.02$, the mesh needs to be (at least) 500 × 2000. Finer mesh is required as the topological disorder increases (reduce in apparent diameter leads to smaller possible $r_{\min}$). After examining all possible cases, we finally choose a mesh of 800 × 3200 to ensure $N_{\min} = 10$ for all simulation cases. The kinematic viscosities for both fluids are 0.1667 lu. The invading and defending fluids have densities of 1 and 0.8 lu, respectively, leading to a viscosity ratio $M = 0.8$. The interfacial tension can be calculated using Young-Laplace equation, which is 0.2152 lu. The invading fluid is injected from the left with a constant velocity of $V_{\mathrm{inj}} = 0.005$ lu, leading to a capillary number $\mathrm{Ca} = \frac{V_{\mathrm{inj}}\mu_{\mathrm{def}}}{\gamma} = 0.0031$. The pore-scale Reynolds number is less than 10. The outlet pressure at the right end is set to be a constant of 0.2667 lu. Periodic boundary condition is applied at top and bottom of the simulation area. Overall, 25 simulations are carried out for five different disorders ($I_v = 0$, 0.020, 0.036, 0.047, 0.054) and five different contact angles ($\theta = 35^\circ$, 62°, 89°, 109°, 128°).

III. RESULTS AND DISCUSSION

The displacement patterns for different wettability conditions and topological disorder are shown in Fig. 3. These are qualitative demonstrations of effects of wettability and disorder on fluid displacement in porous media. Note that these snapshots correspond to the final stage of simulation, which is when the invading fluid reaches the right end of the periodic boundary (see Fig. 1). Generally, stronger fingering and larger trapped area of defending fluid are observed when the medium becomes more disordered (increasing I_v) and more hydrophobic (increasing θ), implying a less efficient displacement, consistent with previous observations [9–12,19–21,23,52]. Figure 3 also demonstrates the "competition" between the destabilizing effect due to uneven distribution of capillary resistance and stabilizing effect from cooperative pore filling events, which have a higher occurrence when contact angle is small. To provide quantitative information about these

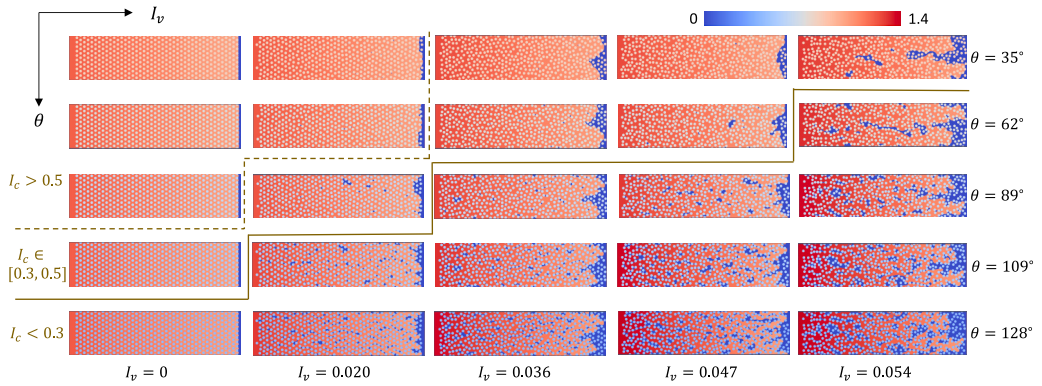

FIG. 3. Displacement patterns (from data of invading fluid) for different disorder (left to right, $I_v = 0,\ 0.020,\ 0.036,\ 0.047,\ 0.054$) and wettability (top to bottom, $\theta = 35°,\ 62°,\ 89°,\ 109°,\ 128°$). The color map represents the density of invading fluid in lattice unit. Note that in LBM, the density fields of invading and defending fluids are stored in separate matrices. Here only the matrix storing data of invading fluid is shown. The blue color (density of invading fluid being zero) stands for the location of defending fluid, and the density fluctuation represents the pressure variation.

patterns, the normalized fluid-fluid interfacial length, $L^* = \frac{\text{interfacial length}}{\text{width of geometry}}$, is calculated and plotted as a function of saturation of invading fluid S for each time-step (Fig. 4). Note that to exclude the boundary effect at outlet we conduct representative volume analysis and found an area of interest with $L_{\text{AOI}} = 3$ well captures the displacement data, so it is within this area (Fig. 1) our results are based on. Figure 4 shows that the rates at which interfacial length increase are larger as the media become more disordered (following the direction of black arrow) for all wettability conditions. This dependence becomes stronger as the contact angle increases, which again can be explained by the stabilizing effect of wettability [20,21]: trapping is mitigated by cooperative pore filling, or overlap, during displacement for disordered media (corresponding to the four collapsed curves for $\theta = 35°$). As the contact angle increases, this "mitigating effect" is reduced such that more trapping events occur, leading to higher interfacial length. Furthermore, we also quantify (a) the residual saturation [Figs. 5(a) and 5(c)] and (b) the ratio of final interfacial length to saturation [Figs. 5(b) and 5(d)] as functions of I_v and θ: increase in I_v and θ leads to decrease in displacement efficiency and increase in interfacial length per unit of saturation. These results again demonstrate the combined impacts of topological disorder and wettability.

To analytically investigate how wettability and disorder cooperate together to influence fluid displacement, we start with the equation that contain the physics of fluid displacement in multiple

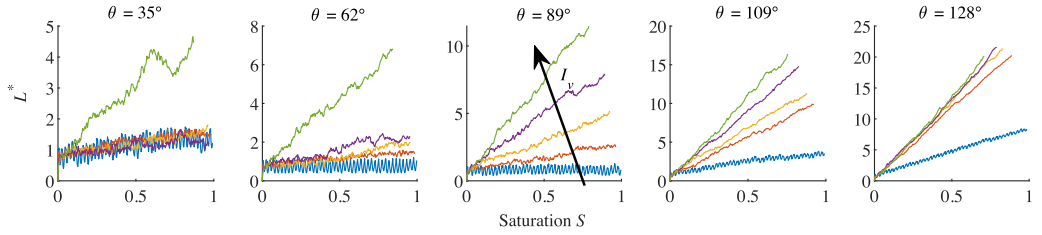

FIG. 4. Normalized fluid-fluid interfacial length (L^*) as a function of saturation of invading fluid (S) for different wettability and topological disorder. The black arrow indicates the direction of increasing disorder: $I_v = 0,\ 0.020,\ 0.036,\ 0.047,\ 0.054$ corresponding to blue, orange, yellow, purple, and green curves, respectively.

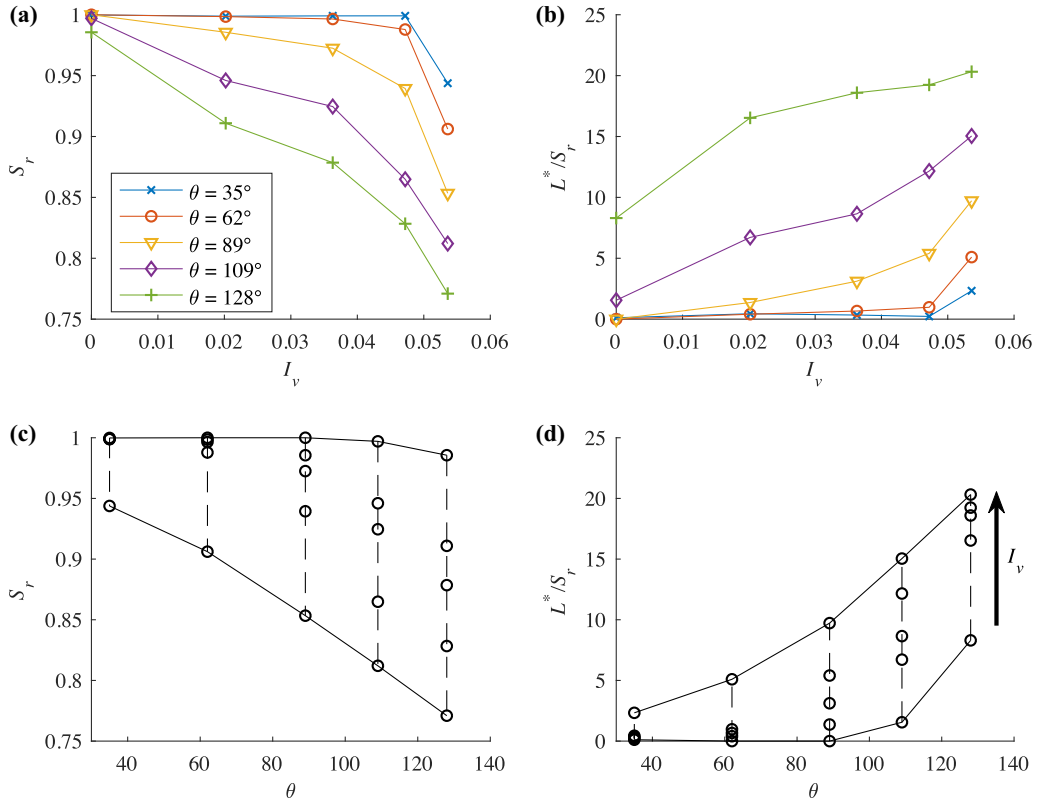

FIG. 5. (a) Final saturation of invading fluid S_r (or displacement efficiency, which is the fraction of defending fluid that has been displaced from the media at the end of the simulation) as a function of I_v and θ. (b) Final normalized interfacial length L^* over final saturation S_r as a function of I_v and θ. (c), (d) Same data set as a function of contact angle θ for different topological disorders. Black arrow indicates the direction of increasing values of I_v from 0 to 0.054.

throats as suggested by Lenormand *et al.* [15]:

$$q = K_1\left(P - P_{c_1}\right)^+ + K_2\left(P - P_{c_2}\right)^+ + \cdots = \sum_{n=1}^{N} K_n\left(P - P_{c_n}\right)^+, \tag{6}$$

where q is is the total flow rate, N is total number of throats, K_n is the hydraulic conductance at local pore throat n, P is the pressure difference of invading and defending fluids, and P_{c_n} is the local capillary pressure providing resistance to the invasion of throat n. Locally, as long as P is smaller than P_{c_n}, there is no displacement. Then, the pressure difference between invading and defending fluids increases as more invading fluid is injected, resulting in $P > P_{c_n}$ at throat n, leading to local throat invasion. Thus, in absence of viscous fingering, it is the uneven distribution of local capillary pressure that leads to uneven invasion of pores and consequent trapping and fingering, which ultimately affects the fluid-fluid interfacial length and displacement efficiency. To calculate the maximum allowable capillary pressure $P_{c,\max}$ before a throat is invaded, we consider three basic pore-scale mechanisms: "burst," "touch," and "overlap" [53]. First, the equation for capillary pressure P_c at throat n in porous medium filled with circular obstacles of same diameter can be calculated by

$$P_{c_n} = \frac{2\gamma \sin(\alpha + \theta - 90^\circ)}{h_n - d\cos(\alpha)}, \tag{7}$$

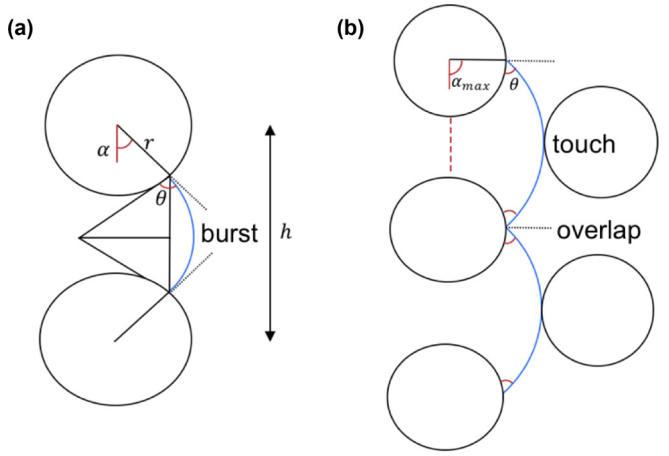

FIG. 6. (a) Schematic figure for calculation of local capillary pressure as a function of center-to-center distance of particle h, radius r, contact angle θ, and filling angle α. (b) Schematic figure for calculation of α_{crit}, which is the maximum allowable α, larger than which the local throat being considered (red dashed line) will be invaded.

where γ is the interfacial tension, h is the center-to-center distance of obstacles, d is the diameter, and α is the filling angle shown in Fig. 6(a). Then, we define that the throat is invaded if (i) the front of invading fluid comes in contact with the next obstacle (touch), or (ii) α reaches α_{overlap} corresponding to cooperative pore filling event (overlap), assuming that obstacles are placed on triangular lattices [Fig. 6(b)]. Thus, for given contact angle θ, the critical angle α_{crit} can be calculated as $\alpha_{\text{crit}} = \min(\alpha_{\text{touch}}, \alpha_{\text{overlap}})$, where α_{touch} is calculated based on θ and $\alpha_{\text{overlap}} = 90^\circ$. Different characteristic front shape indicated by α_{overlap} may be used by other researchers depending on the porosity of the medium [21]. In our study it is found α_{overlap} will not significantly impact the results and 90° is adopted. Finally, for every throat, the $P_{c,\max}$ can be calculated as

$$P_{c,\max} = \max(P_c), \alpha \in [-90^\circ, \alpha_{\text{crit}}], \tag{8}$$

which is the maximum capillary pressure before the front reaches any of the instability state at burst, touch, or overlap. It is found that log-normal curves can well fit most of the $P_{c,\max}$ distributions, and the probability distributions of $P_{c,\max}$ for different I_v and θ are plotted in Fig. 7. It shows that as the medium becomes more disordered, the distribution of $P_{c,\max}$ spreads out. In the meantime, increase in contact angle of invading fluid amplifies this effect, which further increases the variation in $P_{c,\max}$. Thus, the $P_{c,\max}$ distribution captures the interplay among wettability and geometry of

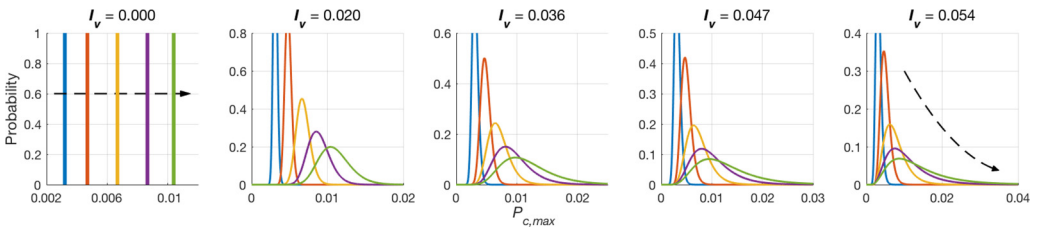

FIG. 7. Probability distribution of local maximum capillary pressure for different disorder and wettability (histogram for $I_v = 0$ and probability density function for log-normal fitting of other values of I_v). Black dashed arrow indicates the direction of increasing contact angle. Blue, orange, yellow, purple, and green colors correspond to $\theta = 35^\circ,\ 62^\circ,\ 89^\circ,\ 109^\circ,\ 128^\circ$, respectively.

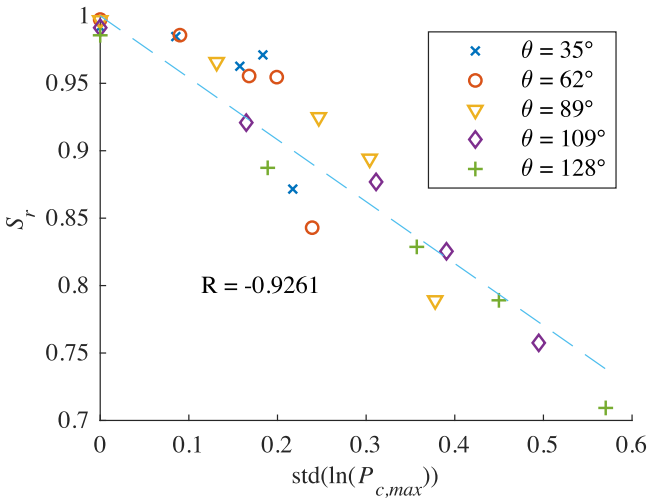

FIG. 8. Final saturation S_r as a function of standard deviation of logarithm maximum capillary pressure for different topological disorder and wettability.

the system, reflecting the resultant capillary resistance, which should have close relationship with the displacement patterns. To validate this hypothesis, the final saturation of invading fluid S_r, or displacement efficiency, is plotted against the standard deviation of $\ln(P_{c,\max})$ in Fig. 8 for all our simulation cases. Collapses of curves for different wettability conditions and disorder can be observed, showing a linear relationship with a correlation coefficient $R = -0.9261$.

On the other hand, regarding the fluid-fluid interfacial length, Liu *et al.* [54] found that the interfacial length L and saturation of invading fluid S can be correlated with a power-law relationship: $L = kS^{\beta}$, where k and β are fitting parameters depending on the geometry. Here, we propose a modified correlation between interfacial length and saturation assuming a power-law relation between normalized interfacial length L^* and "injection length" vt:

$$L^* = \frac{L}{H} = k(vt)^{\beta} = k(\phi W S)^{\beta}, \tag{9}$$

where, v is the injection velocity, t is time, H is the injection width (across which the invading fluid is injected), ϕ is porosity, W is the domain longitudinal length, S is saturation of invading fluid, k and β are parameters that can be estimated based on capillary index I_c depending on system disorder and wettability conditions, which is defined as

$$I_c = \frac{I_{v,\max} - I_v}{I_{v,\max} - I_{v,\min}} \frac{\cos(\theta_{\max}) - \cos(\theta)}{\cos(\theta_{\max}) - \cos(\theta_{\min})}, \tag{10}$$

where $I_{v,\max}$ is the maximum disorder index depending on overall porosity of the geometry and total number of obstacles inside the system, being 0.08 for the current setting. $I_{v,\min} = 0$ is the disorder index for fully ordered system. $\cos(\theta_{\max})$ and $\cos(\theta_{\min})$ are -1 and 1, corresponding to $\theta = 180^{\circ}$ and $\theta = 0^{\circ}$, respectively. As we have discussed previously that increase in contact angle and topological disorder promotes fingering, therefore, I_c is a direct indicator of the collaborative effect due to medium geometry and wettability conditions. A small value of I_c implies relatively large θ and I_v, which leads to less efficient displacement, while larger values of I_c would correspond to more stable displacement. We plot the parameters β and $\ln(k)$ from Eq. (10) as function of I_c in Fig. 9(a) and found that with $I_c < 0.5$, both β and $\ln(k)$ show a strong linear relation with I_c, having R of -0.9467 and 0.9958, respectively. For $I_c \geqslant 0.5$, the displacement patterns are all stable, resulting in small β and large $\ln(k)$, indicating weak dependence of L^* on S_r: L^* is only composed of the

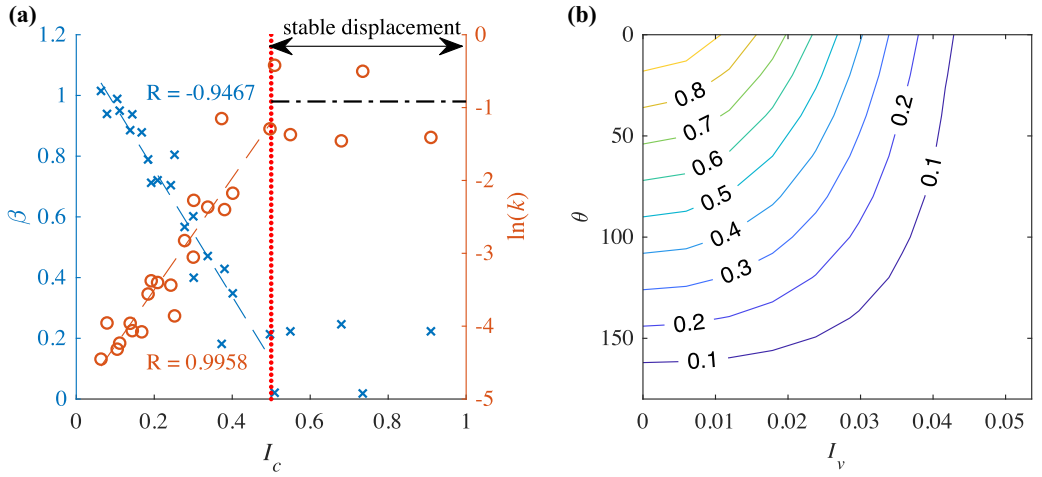

FIG. 9. (a) β (blue cross) and $\ln(k)$ (orange circle) in Eq. (9) as a function of I_c. The blue dashed line and orange solid line are the best fit lines for β and $\ln(k)$, respectively. Black dashed line indicates the theoretical value for $\ln(k)$ in perfect stable displacement. (b) Contour plot of I_c as functions of topological disorder (I_v) and wettability (θ).

fluid front, being almost constant during the stable displacement. In Fig. 9(a), the black dashed line and a value of 0 correspond to the theoretical values for $\ln(k)$ and β for perfect stable displacement. Clearly, it can be seen that I_c can also be used to classify displacement patterns Fig. 9(b). As shown in Fig. 3, 25 patterns are separated into three regions by the dashed line ($I_c = 0.5$) and solid line ($I_c = 0.3$) depending on the values of I_c. A smaller value of I_c implies larger interfacial length per unit of saturation. Note for the left-bottom displacement pattern in Fig. 3, if we zoom in and observe carefully, trapping event actually occurs at every obstacle during which small bubbles are formed, leading to much larger interfacial length between fluids than it appears to be. Overall, the proposed power-law relation [Eq. (9)] together with capillary index I_c [Eq. (10)] provide a rigorous method to capture the quantitative relation between L^* and S_r for different disorder and wettability conditions, offering a reasonable way to predict the value of interfacial length.

In the current study, to focus on the effects of disorder and its coupling with wettability on fluid displacement in porous media, the injecting velocity in all simulations are the same, implying a constant capillary number Ca. Although the influence of Ca is not investigated, based on numerous past works, since it is the uneven distribution of capillary pressure that leads to unstable displacement, a decrease in Ca would make all the displacement patterns shown in Fig. 3 more unstable since the capillary effect would become more significant. We also limit our attention to situations where Saffman-Taylor instability, or viscous fingering, is not present by setting the viscosity ratio $M = 0.8$.

IV. CONCLUSION

We systematically study the impact of topological disorder and its coupling with wettability on multiphase flow in porous media via fluid-fluid displacement simulation using lattice Boltzmann method. It has been shown that the disorder of porous media and wettability play a significant role on the fluid-fluid displacement patterns. In addition to the overall porosity of the medium, the consideration of an appropriate "disorder index" is required to capture the effects of microstructure on fluid displacement. The modified disorder index I_v is able to characterize geometries with different disorder by reflecting the degree of fluctuation of local porosity based on Voronoi diagram. Our results show larger contact angle and increasing disorder promote fingering, leading

to larger fluid-fluid interfacial area and lower displacement efficiency. To analytically investigate how wettability and disorder collaboratively influence displacement, we calculate the maximum allowable local capillary pressure $P_{c,\max}$ based on three pore-scale mechanisms during displacement: burst, touch, and overlap. It is found that the standard deviation of $\ln(P_{c,\max})$ strongly correlates with the displacement efficiency for all wettability conditions and disorder. We proposed a more general power-law relation and defined the capillary index I_c, which offers a rigorous way to capture the quantitative relation between L^* and S_r for different disorder and wettability conditions.

While in current work we only consider obstacles of same size, for media with different sizes of grains, modified Voronoi diagram can be adopted to generate the disorder index by taking the varying radii into account. We provide qualitative and quantitative insight into how geometrical features and wettability conditions collaboratively impact the fluid displacement, paving the way for further study of disorder and wettability control on multiphase flow in porous media.

ACKNOWLEDGMENTS

This work was financially supported by Australian Research Council (Project No. DP170102886) and The University of Sydney SOAR Fellowship. Y.G. acknowledges the financial support of Labex MMCD(Grant No. ANR-11-LABX-022-01) for his stay at Laboratoire Navier at ENPC. This research was undertaken with the assistance of the HPC service at The University of Sydney.

[1] M. L. Szulczewski, C. W. MacMinn, H. J. Herzog, and R. Juanes, Lifetime of carbon capture and storage as a climate-change mitigation technology, Proc. Natl. Acad. Sci. USA **109**, 5185 (2012).

[2] J. M. Matter, M. Stute, S. Ó. Snæbjörnsdottir, E. H. Oelkers, S. R. Gislason, E. S. Aradottir, B. Sigfusson, I. Gunnarsson, H. Sigurdardottir, E. Gunnlaugsson, G. Axelsson, H. A. Alfredsson, D. Wolff-Boenisch, K. Mesfin, Diana Fernandez de la Reguera Taya, J. Hall, K. Dideriksen, and W. S. Broecker, Rapid carbon mineralization for permanent disposal of anthropogenic carbon dioxide emissions, Science **352**, 1312 (2016).

[3] L. W. Lake and Society of Petroleum Engineers (US), *Fundamentals of Enhanced Oil Recovery*, SPE continuing education (SPE, Richardson, TX, 1986).

[4] M. Blunt, F. J. Fayers, and F. M. Orr, Carbon dioxide in enhanced oil recovery, Energy Convers. Manage. **34**, 1197 (1993).

[5] F. Nadim, G. E. Hoag, S. Liu, R. J. Carley, and P. Zack, Detection and remediation of soil and aquifer systems contaminated with petroleum products: An overview, J. Petroleum Sci. Eng. **26**, 169 (2000).

[6] J. Lipiec, J. Kuś, A. Słowińska-Jurkiewicz, and A. Nosalewicz, Soil porosity and water infiltration as influenced by tillage methods, Soil Tillage Research **89**, 210 (2006).

[7] B. Dong, Y. Y. Yan, W. Li, and Y. Song, Lattice Boltzmann simulation of viscous fingering phenomenon of immiscible fluids displacement in a channel, Comput. Fluids **39**, 768 (2010).

[8] C. Zhang, M. Oostrom, T. W. Wietsma, J. W. Grate, and M. Warner, Influence of viscous and capillary forces on immiscible fluid displacement: Pore-scale experimental study in a water-wet micromodel demonstrating viscous and capillary fingering, Energy Fuels **25**, 3493 (2011).

[9] H. Liu, A. J. Valocchi, Q. Kang, and C. Werth, Pore-scale simulations of gas displacing liquid in a homogeneous pore network using the lattice Boltzmann method, Transp. Porous Media **99**, 555 (2013).

[10] M. Cieplak and M. O. Robbins, Influence of contact angle on quasistatic fluid invasion of porous media, Phys. Rev. B **41**, 11508 (1990).

[11] B. Dong, Y. Y. Yan, W. Z. Li, and Y. C. Song, Simulation of the influence of surface wettability on viscous fingering phenomenon in porous media, J. Bion. Eng. **7**, 267 (2010).

[12] B. Zhao, C. W. MacMinn, and R. Juanes, Wettability control on multiphase flow in patterned microfluidics, Proc. Natl. Acad. Sci. USA **113**, 10251 (2016).

[13] J.-D. Chen and D. Wilkinson, Pore-Scale Viscous Fingering In Porous Media, Phys. Rev. Lett. **55**, 1892 (1985).
[14] G. M. Homsy, Viscous fingering in porous media, Annu. Rev. Fluid Mech. **19**, 271 (1987).
[15] R. Lenormand, E. Touboul, and C. Zarcone, Numerical models and experiments on immiscible displacements in porous media, J. Fluid Mech. **189** 165 (1988).
[16] C. Cottin, H. Bodiguel, and A. Colin, Drainage in two-dimensional porous media: From capillary fingering to viscous flow, Phys. Rev. E **82**, 046315 (2010).
[17] C. Odier, B. Levache, E. Santanach-Carreras, and D. Bartolo, Forced Imbibition in Porous Media: A Fourfold Scenario, Phys. Rev. Lett. **119**, 208005 (2017).
[18] Y. C. Yortsos, B. Xu, and D. Salin, Phase Diagram of Fully Developed Drainage in Porous Media, Phys. Rev. Lett. **79**, 4581 (1997).
[19] M. Jung, M. Brinkmann, R. Seemann, T. Hiller, M. Sanchez de La Lama, and S. Herminghaus, Wettability controls slow immiscible displacement through local interfacial instabilities, Phys. Rev. Fluids **1**, 074202 (2016).
[20] M. Trojer, M. L. Szulczewski, and R. Juanes, Stabilizing Fluid-Fluid Displacements in Porous Media Through Wettability Alteration, Phys. Rev. Appl. **3**, 054008 (2015).
[21] R. Holtzman and E. Segre, Wettability Stabilizes Fluid Invasion into Porous Media Via Nonlocal, Cooperative Pore Filling, Phys. Rev. Lett. **115**, 164501 (2015).
[22] H. Liu, Y. Zhang, and A. J. Valocchi, Lattice Boltzmann simulation of immiscible fluid displacement in porous media: Homogeneous versus heterogeneous pore network, Phys. Fluids **27**, 052103 (2015).
[23] R. Holtzman, Effects of pore-scale disorder on fluid displacement in partially-wettable porous media, Sci. Rep. **6**, 36221 (2016).
[24] T. Pak, I. B. Butler, S. Geiger, M. I. J. van Dijke, and K. S. Sorbie, Droplet fragmentation: 3D imaging of a previously unidentified pore-scale process during multiphase flow in porous media, Proc. Natl. Acad. Sci. USA **112**, 1947 (2015).
[25] R. Holtzman and R. Juanes, Crossover from fingering to fracturing in deformable disordered media, Phys. Rev. E **82**, 046305 (2010).
[26] C. Zhang, M. Oostrom, J. W Grate, T. W Wietsma, and M. Warner, Liquid CO_2 displacement of water in a dual-permeability pore network micromodel, Environ. Sci. Technol. **45**, 7581 (2011).
[27] W. Xu, J. T. Ok, F. Xiao, K. B. Neeves, and X. Yin, Effect of pore geometry and interfacial tension on water-oil displacement efficiency in oil-wet microfluidic porous media analogs, Phys. Fluids **26**, 093102 (2014).
[28] B. K. Primkulov, S. Talman, K. Khaleghi, A. R. Shokri, R. Chalaturnyk, B. Zhao, C. W. MacMinn, and R. Juanes, Quasistatic Fluid-Fluid Displacement in Porous Media: Invasion-Percolation Through a Wetting Transition, Phys. Rev. Lett. **3**, 104001 (2018).
[29] M. Blunt and P. King, Relative permeabilities from two- and three-dimensional pore-scale network modeling, Transp. Porous Media **6**, 407 (1991).
[30] M. S. Al-Gharbi and M. J. Blunt, Dynamic network modeling of two-phase drainage in porous media, Phys. Rev. E **71**, 016308 (2005).
[31] M. Ferer, C. Ji, G. S. Bromhal, J. Cook, G. Ahmadi, and D. H. Smith, Crossover from capillary fingering to viscous fingering for immiscible unstable flow: Experiment and modeling, Phys. Rev. E **70**, 016303 (2004).
[32] S. Osher and J. A. Sethian, Fronts propagating with curvature-dependent speed: Algorithms based on Hamilton-Jacobi formulations, J. Comput. Phys. **79**, 12 (1988).
[33] H. Huang, P. Meakin, and M. Liu, Computer simulation of two-phase immiscible fluid motion in unsaturated complex fractures using a volume of fluid method, Water Resour. Res. **41**, 22 (2005).
[34] A. Q. Raeini, M. J. Blunt, and B. Bijeljic, Modelling two-phase flow in porous media at the pore scale using the volume-of-fluid method, J. Comput. Phys. **231**, 5653 (2012).
[35] H. A. A. Amiri and A. A. Hamouda, Evaluation of level set and phase field methods in modeling two phase flow with viscosity contrast through dual-permeability porous medium, Int. J. Multiphase Flow **52**, 22 (2013).

[36] H. S. Rabbani, D. Or, Y. Liu, C.-Y. Lai, N. B. Lu, S. S. Datta, H. A. Stone, and N. Shokri, Suppressing viscous fingering in structured porous media, Proc. Natl. Acad. Sci. USA **115**, 4833 (2018).
[37] W. Shyy, R. W. Smith, H. S. Udaykumar, and M. M. Rao, *Computational Fluid Dynamics with Moving Boundaries* (Taylor & Francis, Bristol, PA, 1996).
[38] X. Shan and H. Chen, Lattice Boltzmann model for simulating flows with multiple phases and components, Phys. Rev. E **47**, 1815 (1993).
[39] X. Shan and G. Doolen, Multicomponent lattice-Boltzmann model with interparticle interaction, J. Stat. Phys. **81**, 379 (1995).
[40] Z. Guo and T. S. Zhao, Lattice Boltzmann model for incompressible flows through porous media, Phys. Rev. E **66**, 036304 (2002).
[41] H. A. A. Amiri and A. A. Hamouda, Pore-scale modeling of nonisothermal two phase flow in 2D porous media: Influences of viscosity, capillarity, wettability, and heterogeneity, Int. J. Multiphase Flow **61**, 14 (2014).
[42] T. Kruger, H. Kusumaatmaja, A. Kuzmin, O. Shardt, G. Silva, and E. M. Viggen, *LBM—The Principles and Methods* (Springer, Berlin, 2017).
[43] F. Diotallevi, L. Biferale, S. Chibbaro, A. Lamura, G. Pontrelli, M. Sbragaglia, S. Succi, and F. Toschi, Capillary filling using lattice Boltzmann equations: The case of multiphase flows, Eur. Phys. J. Special Topics **166**, 111 (2009).
[44] L. Chen, Q. Kang, Y. Mu, Ya-Ling He, and Wen-Quan Tao, A critical review of the pseudopotential multiphase lattice Boltzmann model: Methods and applications, Int. J. Heat Mass Transf. **76**, 210 (2014).
[45] H. Liu, Q. Kang, C. R. Leonardi, S. Schmieschek, A. Narvaez, B. D. Jones, J. R. Williams, A. J. Valocchi, and J. Harting, Multiphase lattice Boltzmann simulations for porous media applications, Comput. Geosci. **20**, 777 (2015).
[46] H. Laubie, F. Radjai, R. Pellenq, and F.-J. Ulm, Stress Transmission and Failure in Disordered Porous Media, Phys. Rev. Lett. **119**, 075501 (2017).
[47] O. Borgman, P. Fantinel, W. Lühder, L. Goehring, and R. Holtzman, Impact of spatially correlated pore-scale heterogeneity on drying porous media, Water Resour. Res. **53**, 5645.
[48] H. Huang, D. T. Thorne, M. G. Schaap, and M. C. Sukop, Proposed approximation for contact angles in Shan-and-Chen-type multicomponent multiphase lattice Boltzmann models, Phys. Rev. E **76**, 066701 (2007).
[49] J. Latt and B. Chopard, Lattice Boltzmann method with regularized nonequilibrium distribution functions, Math. Comput. Simul. **72**, 165 (2006).
[50] A. A. Mohamad, *LBM—Fundamentals and Engineering Applications with Computer Codes* (Springer, Berlin, 2011).
[51] P. Raiskinmäki, A. Shakib-Manesh, A. Jäsberg, A. Koponen, J. Merikoski, and J. Timonen, Lattice-Boltzmann simulation of capillary rise dynamics, J. Stat. Phys. **107**, 143 (2002).
[52] H. Ran, W. Jiamin, Y. Zhibing, C. Yi-Feng, and T. Tetsu, Wettability and flow rate impacts on immiscible displacement: A theoretical model, Geophys. Res. Lett. **45**, 3077 (2018).
[53] M. Cieplak and M. O. Robbins, Dynamical Transition in Quasistatic Fluid Invasion in Porous Media, Phys. Rev. Lett. **60**, 2042 (1988).
[54] H. Liu, A. J. Valocchi, C. Werth, Q. Kang, and M. Oostrom, Pore-scale simulation of liquid CO_2 displacement of water using a two-phase lattice Boltzmann model, Adv. Water Resour. **73**, 144 (2014).